Microstructure of cobalt oxide doped sintered ceria solid solutions

Eva Jud · Zaoli Zhang · Wilfried Sigle ·
Ludwig J Gauckler

Abstract The sintering of ceria solid solutions, such as $Ce_{0.9}Gd_{0.1}O_{1.95}$ (CGO10), is strongly promoted by the addition of 1 cat% of cobalt oxide, lowering the maximum sintering temperature by 200°C and triplicating the maximum densification rate. This change in sintering behavior results from cobalt ion segregated at the grain boundaries. An average cobalt ion boundary coverage is at maximum 3.0 ± 1.9 at/nm^2 and is shown to depend on the cooling rate. Coverage by segregated gadolinium is also found and amounts to 13.2 ± 11.4 at/nm^2 for a slowly cooled sample. From cobalt excess measured at the boundary, an estimated concentration of only 0.06 cat% of cobalt oxide is necessary to promote the sintering effect. The remaining amount of cobalt oxide is found in triple points and as particles in clusters. It is expected that the amount of cobalt oxide necessary for fast densification can be reduced with a doping process that distributes the additives more homogeneously.

Keywords Ion conductor · Electrolyte · Cobalt oxide doping · Grain boundary segregation · Grain boundary excess

1. Introduction

It is a long-standing objective of Solid Oxide Fuel Cell (SOFC) technology to reduce the cost of operation as well as that of production. Lowering the operation temperature while maintaining equal efficiency represents the most promising strategy to this end. This means to replace the standard yttria-stabilized zirconia (YSZ) electrolyte with a material of higher ionic conductivity. Ceria solid solutions offer four to five

E. Jud (✉) · Z. Zhang · W. Sigle · L. J. Gauckler
Dept. of Materials Science and Engineering, 77 Massachusetts
Avenue, Cambridge, MA 02139, USA
e-mail: ejud@mit.edu

times higher ionic conductivity at intermediate temperatures (500–800°C) and have been extensively studied [1–5]. In particular, $Ce_{1-x}Gd_xO_{2-x/2}$ electrolytes possess a high ionic conductivity [5–11].

Fabrication of gas-tight ceria electrolytes, i.e. relative density >0.95, requires sintering temperatures >1300°C. The use of transition metal oxides (e.g. cobalt oxide) as sintering aid for $Ce_{0.8}Gd_{0.2}O_{1.9}$ (CGO20) and $Ce_{0.9}Gd_{0.1}O_{1.95}$ (CGO10) results in much lower sintering temperatures (900°C), higher shrinkage rates, and grain sizes in the submicron range ($\sim$120 nm) [12, 13]. The most effective doping concentration was reported to be 2 cat% of cobalt oxide. Higher doping concentrations or higher temperatures lead to detrimental sintering effects [14, 15]. Further, the addition of cobalt oxide to CeO_2 [16] and CGO20 [17] results in a higher grain growth rate compared to undoped ceria solid solutions. The oxygen ion conductivity was reported as unchanged upon addition of cobalt oxide to CGO20 [12]. Lewis et al. measured a higher lattice conductivity in doped CGO10, which was assigned to the formation of additional oxygen vacancies due to the substitution of Co^{3+} for Ce^{4+} resulting in a minimum lattice parameter change [18]. Fagg et al. reported that the total electrical conductivity of 2 cat% cobalt oxide doped CGO20 remains unchanged as long as sintering is performed between 900 and 1000°C. Increased p-type conductivity was detected in doped samples and a decrease of the oxygen ion transference number from 0.99 to 0.89 was determined for doped samples sintered between 650 and 1000°C [19].

Improved sintering characteristics were first assigned to the formation of a thin amorphous cobalt rich grain boundary film, which disappears at higher sintering temperature and/or with increasing dwell time [12]. This observation was later refuted by Lewis et al. who found significant cobalt concentration at the boundary even after a dwell of 12 h at 980°C

[18]. Enriched cobalt oxide boundary layers were further confirmed for CGO20 samples at 900°C, but distinct areas of higher cobalt oxide concentration were detected as well [19]. The existence of cobalt oxide in the grain boundary after long dwell times has recently been confirmed again on the basis of conductivity measurements [20].

The example of cobalt oxide doped CGO shows that dopants exert a strong influence upon various properties, such as sintering, grain growth, conductivity, and microstructure. The most prominent example certainly is the addition of small amounts of MgO to Al_2O_3 preventing exaggerated grain growth [21]. Another example is the influence of Y_2O_3 doping on the densification and grain growth of Al_2O_3 [22]. Three distinct regimes were observed in the adsorption process of Y to the grain boundaries of alumina [23]. First, for low dopant concentrations (<100 ppm), a simple McLean-Langmuir adsorption isotherm was found. By increasing the dopant concentration, a regime of grain boundary supersaturation was identified indicating that a nucleation barrier exists for the precipitation of yttrium aluminate garnet (YAG). For Y_2O_3 addition exceeding 700 ppm, YAG precipitates in grain boundary triple points and a constant coverage of Y at the grain boundaries was found.

In the understanding of the microstructural evolution of doped ceramics, background impurities, such as SiO_2, are of major concern [24, 25]. In case of electrolyte materials for SOFC, trace amounts of SiO_2 can easily increase the grain boundary electrical resistance by several orders of magnitude in YSZ [25–27] as well as CGO [28]. Consequently, the total resistance is dominated by the impurities whose occurrence becomes especially important in the context of lowering the operation temperature of SOFCs. A straightforward method to exclude impurities is of course the use of highly pure starting powders. However, in order to minimize cost, the use of commercially available powder is generally preferred, which in turn inevitably contain a certain amount of trace impurities. Since segregation at grain boundaries is grain size dependent, the fabrication of electrolytes with small grain sizes represents an option to reduce impairing effects of impurity segregation. Yet, the introduction of impurities during processing should be carefully avoided.

Although the effect of transition metal oxides on the densification, grain growth, and conductivity of ceria solid solutions has been confirmed many times, the exact mechanism is still under debate [12, 18–19, 29, 30]. In the present study, an attempt has been made to elucidate the microstructural evolution of cobalt oxide in CGO during sintering in order to get insights into the distribution and the effect of the dopant.

2. Experimental procedures

Commercially available $Ce_{0.8}Gd_{0.2}O_{1.9}$ (CGO20) and $Ce_{0.9}Gd_{0.1}O_{1.95}$ (CGO10) powders were used (Rhodia Elec-

tronics & Catalysis, France). Particle sizes were determined by BET adsorption measurements (Nova1000, Quantachrome, Germany), scanning electron microscopy (SEM) (LEO 1530, Germany), transmission electron microscopy (TEM), and X-ray diffraction (XRD—Diffractometer D 5000, Siemens, Germany) combined with Rietveld refinement (TOPAS R 2.0, Bruker AXS, Germany). CGO was doped with cobalt oxide by dispersing the powder ultrasonically in ethanol and by adding the desired amount of cobalt nitrate hexahydrate (Fluka Chemie GmbH, Switzerland) dissolved in ethanol. The suspension was dried at 120°C and ground in an agate mortar. Calcination at 400°C for 2 h decomposed the cobalt nitrate into cobalt oxide. Undoped and doped CGO powder was isostatically pressed at 300 MPa for 3 min yielding cylindrical green bodies with a diameter of about 5 mm. The cylindrical compacts were cut into rods of 10 to 12 mm length. The density was determined before and after sintering using the Archimedes method. The samples were sintered with a constant heating rate using a horizontal dilatometer (Type 802S, Bähr Thermoanalyse GmbH, Germany).

Bright field TEM images were obtained on a Tecnai F30 microscope (FEI) with a field emission gun operated at 300 kV. For elemental mappings by electron spectroscopic imaging (three window technique), an imaging filter (GIF, Gatan) mounted below the microscope column was used. Samples were prepared by crushing and dispersing them onto perforated carbon films supported on copper grids.

For the HRTEM, samples were prepared by first grinding, dimpling, polishing and finally ion milling in a Gatan Duomill [31]. For ion milling, an inclination angle of 12° and an Ar ion energy in the range of 2.5–4 keV was used. The JEOL ARM 1250 microscope with a point-to point-resolution of 0.12 nm was used for the HRTEM studies. The microscope is equipped with a drift compensation system, which helps stabilizing the image.

For analytical TEM, a dedicated STEM (VG HB 501 UX, Vacuum Generators) was used. The microscope was operated at 100 keV. It is equipped with a cold field-emission gun, an energy dispersive X-ray spectrometer (Noran) and an electron energy-loss spectrometer (Gatan UHV ENFINA).

The energy resolution in EELS, as measured by the full width at half maximum of the zero-loss peak, was 0.7 eV. The electron probe size was below 1 nm. The probe currents used were in the range of 0.5–1 nA. Spectra were recorded with a dispersion of 0.5 eV/channel, which allows to simultaneously acquire the Co $L_{2,3}$-edge, Ce M-edge, and Gd M-edge. During the measurement, the grain boundary is as perfect edge on condition as possible. The energy scale for the EELS spectra was calibrated by setting the low-energy Ce white line to 883 eV. The convergence and collection semi-angles were both 6.5 mrad. All data shown here were corrected for dark current and detector gain variation. The spectrum acquisition

and processing were done with the Digital Micrograph 3.6 Spectrum Imaging and EL/P software. The background for each spectrum was subtracted by the fit of a power law function to the pre-edge background [32]. Hartree-Slater cross-sections were used for the quantification.

The Co (and Gd) excess at grain boundaries was measured by a box technique [33]. Using an area of 3×4 nm^2 or 6×8 nm^2. Quantification of the excess is made by determining the difference of the amount of a specific element (here, Co or Gd) found in two regions: first, right on the boundary and second, off the boundary within the nearby bulk region [34–36]. The results are obtained in terms of interfacial excess for each element which is formulated for the case of Co excess at the grain boundary (GB) as:

$$\Gamma_{Co}^{exc} = \frac{\sigma_{Ce}}{\sigma_{Co}} \cdot \omega \cdot n \left(\frac{I_{Co}^{GB} - I_{Co}^{Bulk}}{I_{CE}^{GB}} \right) \tag{1}$$

Here, n is the site density (atoms/unit cell, here, $n = 25.262$ atoms/nm^3), ω the width of the box perpendicular to the boundary, I the EELS edge intensity within the selected energy-loss range, and σ the partial inelastic scattering cross-section corresponding to this energy-loss range.

3. Results and discussion

In the preparative steps of the experiments, especially during the doping process, measures of precaution were taken to avoid introduction of additional impurities. However, the results from laser ablation of pellets sintered in a dedicated clean alumina furnace revealed at least 140 ppm of silicon in CGO10 and CGO20 (Table 1). According to the supplier, Si concentrations should be less than 100 ppm for both powders. In addition, the CGO20 sample exhibited up to 1000 ppm of lanthanum, which probably originates from the precursor used by the powder supplier. Lanthanum is the second most abundant lanthanide after cerium.

Table 1 Average impurity concentrations in sintered CGO10 and CGO20 obtained by laser ablation combined with inductively coupled mass spectroscopy

Element (ppm)	CGO10	CGO20
Si	230	140
La	30	1000
Yb	50	50

Table 2 Powder particle diameters obtained by BET N$_2$ adsorption and by Rietveld refinement

Diameter (nm)	CGO10	CGO20
d_{BET}	23	35
d_{XRD}	20	32

For both powders CGO10 and CGO20, the equivalent particle diameters determined from BET adsorption are consistent with the crystallite sizes calculated by Rietveld refinement (Table 2). Powder CGO10 exhibits a slightly smaller equivalent particle diameter, 23 nm compared to 35 nm for CGO20. These particle size values are confirmed by comparison with SEM and TEM images of powder CGO20 (Fig. 1).

The effect of the dopant cobalt oxide on sintering is clearly demonstrated in Fig. 2. Whereas undoped CGO20 requires temperatures higher than 1200°C for complete densification, cobalt oxide doped CGO20 becomes fully dense at 1000°C. Furthermore, the densification rate is increased by more than a factor of three due to the addition of 1 cat% of cobalt oxide. Whereas the densification rate of undoped CGO slowly decreases after reaching the maximum value, it abruptly falls off for cobalt oxide doped CGO. It is interesting to notice that the start of sintering is actually delayed for doped CGO. Between 750 and 880°C, the shrinkage rate of CGO is higher than that of doped CGO. Although CGO10 possesses a smaller primary particle size than CGO20, it is less sinterable, i.e. it has a lower final density, a higher sintering temperature, and a lower maximum shrinkage rate. This difference is probably due to a less favorable agglomerate structure of the

Fig. 1 CGO20 powder. (a) SEM image of powder agglomerates. (b) Bright field TEM image

(a)　　　　　　　　　　(b)
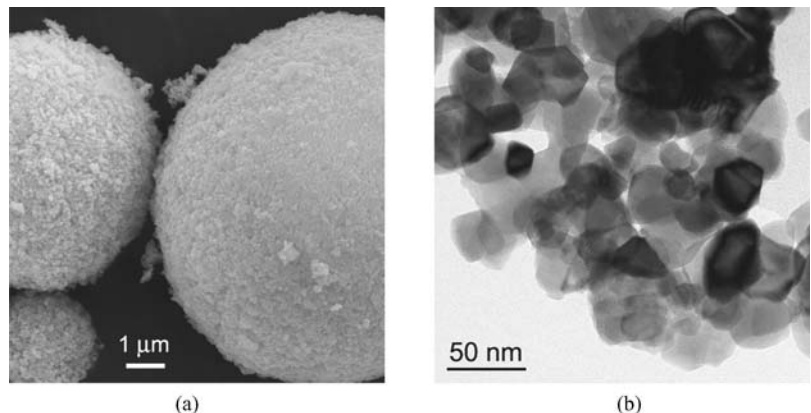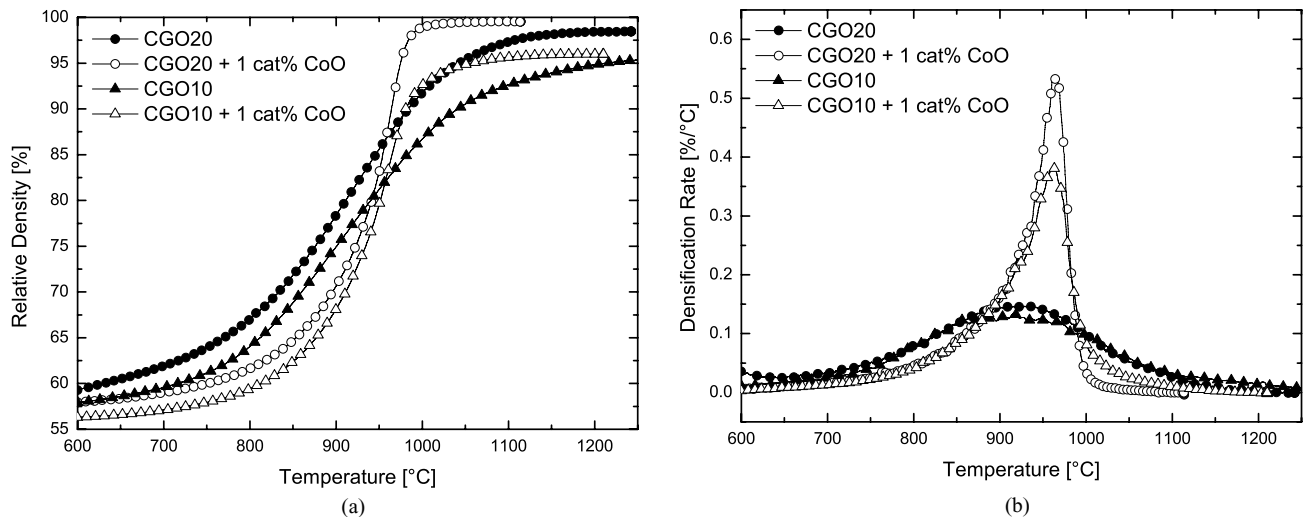
Fig. 2 Sintering behavior at a constant heating rate of 1 °C/min of undoped and cobalt oxide doped CGO10 and CGO20. (a) Relative density as a function of temperature. (b) Densification rate as a function of temperature

Fig. 3 CGO20 doped with 2 cat% of cobalt oxide sintered at 800°C for 2 h. (a) Bright field image. (b) Elemental mapping at Co L$_{2,3}$-edge (white)

(a)   (b)
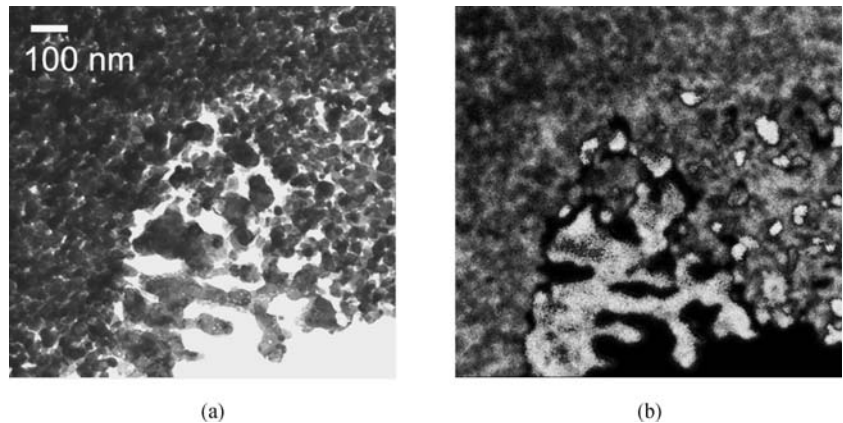
powder CGO10, which is also demonstrated by a lower green density, namely 56.7% for CGO10 and 57.8% for CGO20. Another reason for the lower sinterability might also be the lower concentration in Gd. Nevertheless, the effect of cobalt is obvious and the maximum shrinkage rate in cobalt oxide doped CGO10 and CGO20 occurs at the same temperature of 960°C.

Figure 3 shows a bright field image and an elemental mapping using the Co-L$_{2,3}$ edge of a 2 cat% doped CGO20 powder. The corresponding green body was sintered to 800°C, dwelled for 2 h and air quenched. The elemental mapping shows that at 800°C, which is the temperature where the densification rate starts to increase, cobalt oxide is mainly present as isolated particles combined to clusters. The particle diameter ranges between 10 and 50 nm. Hence, it is unlikely that cobalt oxide forms a film around the powder particles before sintering. The elemental mapping in Fig. 3 shows rather clearly that the doping process produces a quite inhomogeneous distribution of the dopant. At higher tem-

peratures, namely at 900°C, cobalt oxide is still present in the form of particles and they are distributed in the CGO10 matrix (Fig. 4). Since no common phase between cobalt oxide and CGO has been found, it is assumed that the phase of cobalt oxide corresponds to Co$_3$O$_4$ at temperatures lower than 900°C and changes to CoO at temperatures higher than 900°C [37]. From the bright field image in Fig. 4(a), it can be derived that the particle size of cobalt oxide did not change significantly compared to that shown in the mapping presented in Fig. 3(b). However, the CGO10 matrix exhibits a certain grain growth as the grain diameters range between 80 to 120 nm. This grain growth is not surprising since the sintering process is almost complete at 900°C. Similar grain sizes in fully dense CGO have been measured previously even though the powder contained 20 at% of Gd [12, 17].

The image in Fig. 5 shows additionally that cobalt oxide is present as particles in the triple points with an approximate particle diameter from 5 to 10 nm. Larger particles (30 to 100 nm) in triple points have only been found at higher

Fig. 4 CGO10 + 5 cat% of cobalt oxide sintered at 900°C for 2 h and quenched. (a) TEM Bright field image. (b) Elemental mapping at the Co L edge


(a)

(b)
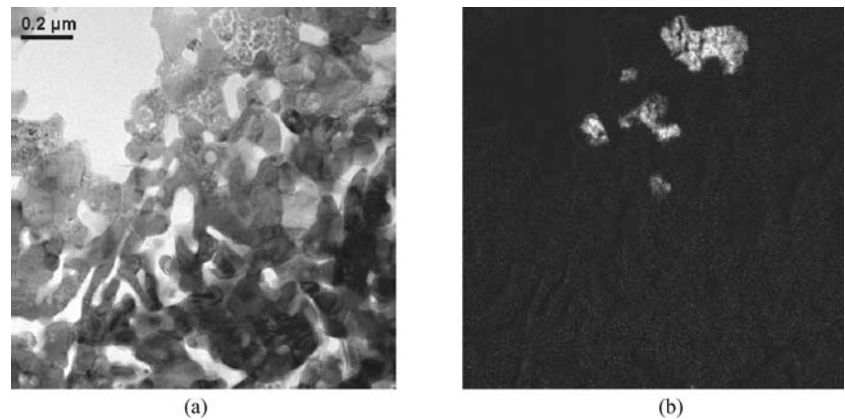
temperatures, i.e. in a sample dwelled at 1150°C for 24 h. At 900°C, the shape of the particles ranges from angular to ovoid and the measured dihedral angles lie between 50 and 120°. Dihedral angles observed in TEM images typically underestimate the correct value as the particles are in the average not sectioned through their center where the largest dihedral angle is measured. Therefore, the dihedral angle of cobalt oxide is estimated to be approximately 120°C.

Cobalt oxide in the form of isolated particles as shown in Figs. 4 and 5 does not have a significant effect on the sintering of CGO as long as only small concentrations are present. At higher concentrations, i. e. more than 3 cat%, these particles lead to agglomerates in the green body and delay the onset of sintering to higher temperatures [38]. The properties of CGO are mainly influenced by the grain boundary structure, where cobalt oxide is found in the form of a very thin grain boundary layer with a thickness of approximately 0.5 nm (Fig. 6). The grain boundary layer shown in Fig. 6 represents

one example. It is not sure whether all grain boundaries are decorated with such a film. However, the cobalt oxide phase forms a percolating network at temperatures between 900 and 1000°C since an electronic conductivity, attributed to the cobalt oxide phase, has been detected in quenched samples. However, the origin of the electronic conductivity is not due to the grain boundary film in the first place, but to the reduction of cobalt oxide, from Co_3O_4 to CoO [38].

Evidence that cobalt is actually present at the grain boundaries is presented in Fig. 7. Here, the cobalt excess in comparison to the grain interior has been measured in several boundaries. Two different samples are compared. The first samples was sintered at 900°C for 2 h and air quenched, the second sample was sintered identically, but slowly cooled with a rate of −0.5°C/min. Clearly, the slowly cooled sample exhibits a higher cobalt concentration, 3.0 ± 1.9 at/nm² in comparison to 1.3 ± 1.0 at/nm² for the quenched sample. In the additional time available during slow cooling, more cobalt can segregate to the boundaries. However, the difference in Co excess between the slowly cooled sample and the quenched samples is not large and this points to a small solubility of Co in the CGO matrix. Chen et al. studied the solubility of Co in CeO_2 and found a value of 3 mol% at
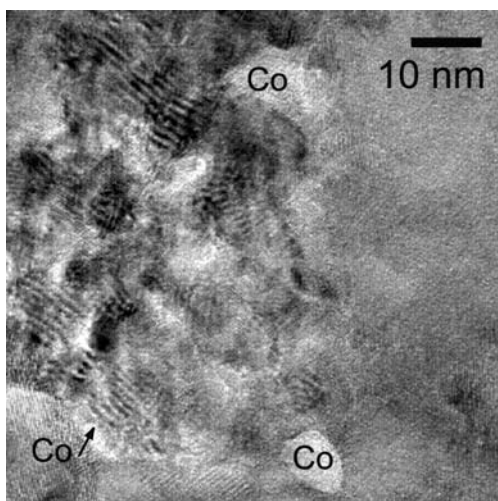
Fig. 5 Cobalt oxide particles in grain boundary triple points in CGO20 doped with 2 cat% of cobalt oxide, sintered for 24 h at 900°C and air quenched
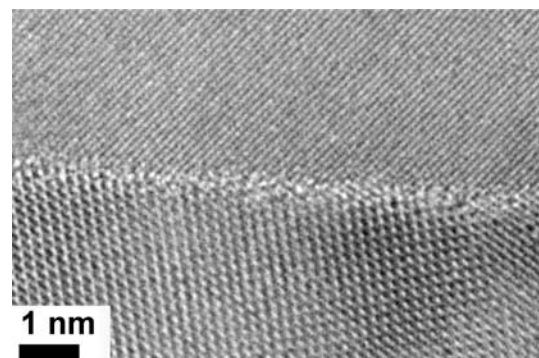
Fig. 6 Cobalt oxide containing grain boundary layer in CGO10 doped with 5 cat% of cobalt oxide, sintered for 2 h at 900°C and cooled with −0.5°C/min
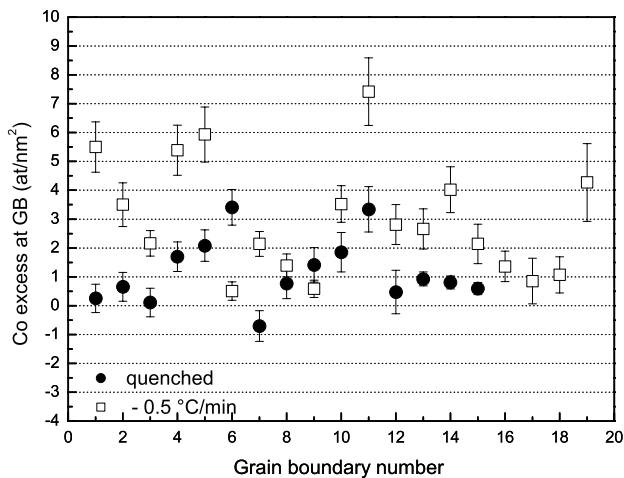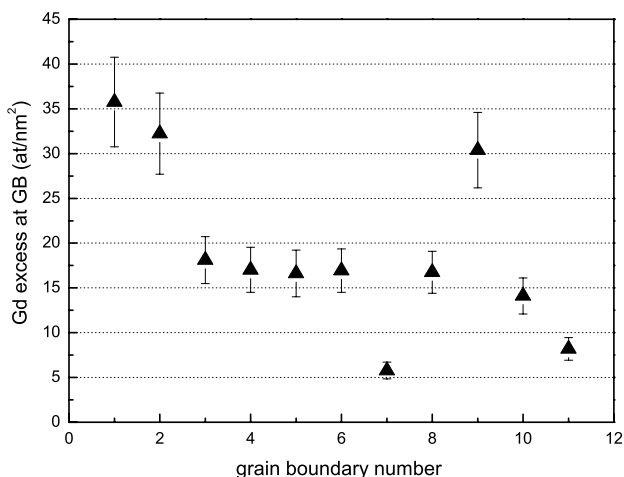
Fig. 7 Co excess at the grain boundary of CGO10 + 5 cat% cobalt oxide sintered at 900°C for 2 h

1580°C [39]. Similarly, the maximum solubility of Co in Gd_2O_3 is less than 2.5 mol% at 1550°C [40]. The maximum solubility of Co in CGO at 900°C can therefore be estimated to be less than 0.5 mol%.

In the case of the slowly cooled sample, the Gd coverage was measured as well (Fig. 8). The mean coverage is found to be 13.2 ± 11.4 at/nm^2, which is significantly higher than that of Co. However, it is important to notice that due to the thin grain boundary layer observed (Fig. 6), Gd ions in the grain boundary near area might have been measured as well. In all three cases (Figs. 7 and 8), the scattering of the measured coverage is quite high. This probably points to the scattering of grain boundary energies generally known in a polycrystalline material.

A higher grain boundary coverage in slowly cooled samples has also been detected by Aoki et al. in CaO-stabilized

Fig. 8 Gd excess at the grain boundary of CGO10 + 5 cat% cobalt oxide sintered at 900°C for 2 h and cooled with −0.5°C/min

ZrO_2, where the Si and Ca coverage was measured [25]. They further showed that impurities can cause significant segregation of divalent and trivalent solvents to the boundary. Similarly, it might be speculated that cobalt oxide causes cosegregation of Gd to the grain boundary. Depending on the amount of Gd in CGO10, different Gd excess levels can be expected at the boundary. As a consequence, the cosegregation of Co and Gd might even be responsible for the superior sintering behavior of CGO20 compared to CGO10 (Fig. 2).

The low solubility of Co in CGO and the low Co excess measured at the boundaries is consistent with the observed large amount of cobalt oxide particles in the CGO matrix as shown in Figs. 4 and 5. The spatial distribution of cobalt oxide can also be confirmed by a simple calculation. For that, the following assumptions are made. First, the solubility of Co is negligible and second, no cobalt oxide precipitation occurs, i.e. cobalt oxide completely adsorbs at the boundary. According to Gülgün et al. [23], the planar density of cobalt at the boundary, Γ can then be calculated as:

$$\Gamma = \frac{GX_t}{3\Omega} \tag{2}$$

where G is the grain size, X_t the total concentration of Co in CGO10, and Ω the volume per cation in CGO (0.01314 nm^3/cat). The volume per cation in CGO20 has been estimated as one third of the atomic volume of CGO20 and represents an upper limit. In case of the investigated TEM samples with a doping concentration of 5 cat% of cobalt oxide and an estimated grain size of 200 nm, the hypothetical grain boundary excess of Co is at least 250 cat/nm^2. Assuming that the boundary consists purely of Co_3O_4, its coverage corresponds to a boundary thickness of roughly 5.5 nm. However, the measured Co excess (Fig. 7) and the observed boundary thickness (Fig. 5) are much lower, which in turn explains the significant number of cobalt oxide particles in the CGO matrix (Fig. 4). On the other hand, if the total concentration of cobalt oxide is calculated with Equation 2, and based on the measured Co excess of 3.0 at/nm^2 in the slowly cooled sample, a value of 0.06 cat% is derived. Assuming that the solubility of cobalt oxide in CGO is negligible, only a very small amount of cobalt oxide at the boundary is already sufficient in order to change the properties of CGO impressively. The calculated concentration of 0.06 cat% is significantly smaller than the concentration of 1 cat%, which was used in the samples for the dilatometric measurements as shown in Fig. 2. Therefore, it can be expected that the favorable effect of cobalt oxide can be achieved at a much lower concentration provided that the dopant is distributed more homogeneously. As a matter of fact, the same conclusion has already been obtained by varying the particle size of the CGO powder [38].

4. Conclusion

Cobalt oxide in small amounts is an effective sintering aid for $Ce_{0.8}Gd_{0.2}O_{1.9}$ (CGO20) and $Ce_{0.9}Gd_{0.1}O_{1.95}$ (CGO10). A dopant concentration of 1 cat% decreases the maximum sintering temperature by roughly 200°C and the maximum shrinkage rate is increased by a factor of three. Interestingly, the temperature of maximum shrinkage rate is independent of the Gd content and lies for CGO20 and CGO10 at around 960°C. The doping process used in the present work results in a rather inhomogeneous distribution of clusters of cobalt oxide which remain present up to 800°C, i.e. the temperature where the shrinkage rate starts to increase significantly. At 900°C, cobalt oxide diffuses into the grain boundaries where it forms, in combination with Gd, a grain boundary film of roughly 0.5 nm thickness. The Co excess at the boundary is a function of the cooling rate. The lower the cooling rate, the more cobalt can segregate to the boundary. In a slowly cooled sample, the average Co excess was found to be 3.0 ± 1.9 at/nm^2 while the Gd excess was measured as 13.2 ± 11.4 at/nm^2. Cobalt oxide is also found in the form of clustering particles or in the triple points of the CGO matrix. For the latter, the particle diameter lies between 5 and 10 nm at 900°C and the dihedral angle is approximately 120°. The cobalt oxide particles are a result of supersaturation as the solubility of cobalt oxide in CGO is estimated to be less than 0.5 mol% at 900°C. Based on the measured Co excess, the essentially required amount of cobalt oxide for promoting the sintering process is calculated as 0.06 cat%. Since this is much less than the actually used amount of dopant (1 cat%), it is inferred that improving the doping process would allow to reduce the amount of dopant, so that cobalt oxide precipitation can be avoided.

References

1. N.Q. Minh, *J. Am. Ceram. Soc.*, **76**, 563 (1993).
2. M. Gödickemeier and L.J. Gauckler, *J. Electrochem. Soc.*, **145**, 414 (1998).
3. B.C.H. Steele, *Solid State Ionics*, **129**, 95 (2000).
4. L.J. Gauckler, D. Beckel, B.E. Buergler, E. Jud, U.P. Muecke, M. Prestat, J.L.M. Rupp, and J. Richter, *Chimia*, **58**, 837 (2004).
5. V.V. Kharton, F.M. Figueiredo, L. Navarro, E.N. Naumovich, A.V. Kovalevsky, A.A. Yaremchenko, A.P. Viskup, A. Carneiro, F.M.B. Marques, and J.R. Frade, *J. Mat. Sci.*, **36**, 1105 (2001).
6. D.K. Hohnke, *Solid State Ionics*, **5**, 531 (1981).
7. A. Overs and I. Riess, *J. Am. Cer. Soc.*, **65**, 606 (1982).
8. J. Faber, C. Geoffroy, A. Roux, A. Sylvestre, and P. Abelard, *Appl. Phys. A Mater. Sci. Proc.*, **49**, 225 (1989).
9. K.Q. Huang, M. Feng, and J.B. Goodenough, *J. Am. Ceram. Soc.*, **81**, 357 (1998).
10. S.R. Wang, T. Kobayashi, M. Dokiya, and T. Hashimoto, *J. Electrochem. Soc.*, **147**, 3606 (2000).
11. T.S. Zhang, P. Hing, H.T. Huang, and J. Kilner, *Solid State Ionics*, **148**, 567 (2002).
12. C. Kleinlogel and L.J. Gauckler, *Adv. Mater.*, **13**, 1081 (2001).
13. G.S. Lewis, A. Atkinson, and B.C.H. Steele, In *Fourth European Solid Oxide Fuel Cell Forum*, edited by U. Bossel (Oberrohrdorf, Switzerland, 2000), p. 773.
14. C. Kleinlogel and L.J. Gauckler, *Solid State Ionics*, **135**, 567 (2000).
15. D. Perez-Coll, P. Nunez, D. Marrero-Lopez, J.C.C. Abrantes, and J.R. Frade, *J. Solid State Electrochem.*, **8**, 644 (2004).
16. T.S. Zhang, P. Hing, H.T. Huang, and J. Kilner, *J. Eur. Cer. Soc.*, **22**, 27 (2002).
17. E. Jud, C.B. Huwiler, L.J. Gauckler, *In preparation* (2005).
18. G.S. Lewis, A. Atkinson, B.C.H. Steele, and J. Drennan, *Solid State Ionics*, **152**, 567 (2002).
19. D.P. Fagg, J.C.C. Abrantes, D. Perez-Coll, P. Nunez, V.V. Kharton, and J.R. Frade, *Electrochimica Acta*, **48**, 1023 (2003).
20. E. Jud and L.J. Gauckler, *J. Electroceram.*, **15**, 159 (2005).
21. R.L. Coble, U.S. Patent, 3026210 (1962).
22. R. Voytovych, I. MacLaren, M.A. Gulgun, R.M. Cannon, and M. Ruhle, *Acta Mater.*, **50**, 3453 (2002).
23. M.A. Gulgun, R. Voytovych, I. Maclaren, M. Ruhle, and R.M. Cannon, *Interface Science*, **10**, 99 (2002).
24. R. Gerhardt, A.S. Nowick, M.E. Mochel, and I. Dumler, *J. Am. Ceram. Soc.*, **69**, 647 (1986).
25. M. Aoki, Y.M. Chiang, I. Kosacki, I.J.R. Lee, H. Tuller, and Y.P. Liu, *J. Am. Ceram. Soc.*, **79**, 1169 (1996).
26. M. Godickemeier, B. Michel, A. Orliukas, P. Bohac, K. Sasaki, L. Gauckler, H. Heinrich, P. Schwander, G. Kostorz, H. Hofmann, and O. Frei, *J. Mat. Res.*, **9**, 1228 (1994).
27. Y.L. Liu, S. Primdahl, and M. Mogensen, *Solid State Ionics*, **161**, 1 (2003).
28. R. Gerhardt and A.S. Nowick, *J. Am. Ceram. Soc.*, **69**, 641 (1986).
29. T.S. Zhang, P. Hing, H.T. Huang, and J. Kilner, *J. Mat. Sci.*, **37**, 997 (2002).
30. E. Jud, C.B. Huwiler, and L.J. Gauckler, *J. Am. Cer. Soc.*, **88**, 3013 (2005).
31. A. Strecker, U. Salzberger, and J. Mayer, *Prakt. Metallogr.*, **30**, 482 (1993).
32. R.F. Egerton, *Electron Energy-Loss Spectroscopy in the Electron Microscope*, 2nd ed., (Plenum Press, New York, 1989).
33. H. Gu, R.M. Cannon, and M. Ruhle, *J. Mat. Res.*, **13**, 376 (1998).
34. J.A.S. Ikeda, Y.-M. Chiang, A.J. Garratt-Reed, and J.B. Vander Sande, *J. Am. Ceram. Soc.*, **76**, 2447 (1993).
35. Y.M. Chiang, L.A. Silverman, R.H. French, and R.M. Cannon, *J. Am. Ceram. Soc.*, **77**, 1143 (1994).
36. J. Bruley, I. Tanaka, H.J. Kleebe, and M. Ruhle, *Anal. Chim. Act.*, **297**, 97 (1994).
37. K. Mocala, A. Navrotsky, and D.M. Sherman, *Phys. Chem. Minerals*, **19**, 88 (1992).
38. E. Jud and L.J. Gauckler, *J. Electroceram.*, **14**, 247 (2005).
39. M. Chen, B. Hallstedt, N.A. Grundy, and L.J. Gauckler, *J. Am. Ceram. Soc.*, **86**, 1567 (2003).
40. N.A. Grundy, *private communication* (2004).